Ultramicroscopy 000 (2017) 1–15

Contents lists available at ScienceDirect

Ultramicroscopy

journal homepage: www.elsevier.com/locate/ultramic

Getting the most out of a post-column EELS spectrometer on a TEM/STEM by optimising the optical coupling

Alan J. Craven[a], Hidetaka Sawada[b], Sam McFadzean[a], Ian MacLaren[a,*]

[a] *SUPA School of Physics and Astronomy, University of Glasgow, Glasgow G12 8QQ, UK*
[b] *JEOL UK Ltd., JEOL House, Silver, Court, Watchmead, Welwyn Garden City Herts., AL7 1LT, UK*

ARTICLE INFO

Article history:
Received 16 December 2016
Revised 1 March 2017
Accepted 14 March 2017
Available online xxx

Keywords:
STEM-EELS
Spectrometer collection angle
Optimised EELS spectrometer-column coupling
Maximising EELS energy loss range
EELS spectrum artefacts
Ray tracing

ABSTRACT

Ray tracing is used to find improved set-ups of the projector system of a JEOL ARM 200CF TEM/STEM for use in coupling it to a Gatan 965 Quantum ER EELS system and to explain their performance. The system has a probe aberration corrector but no image corrector. With the latter, the problem would be more challenging. The agreement between the calculated performance and that found experimentally is excellent. At 200 kV and using the 2.5 mm Quantum entrance aperture, the energy range over which the collection angle changes by a maximum of 5% from that at zero loss has been increased from 1.2 keV to 4.7 keV. At lower accelerating voltages, these energy ranges are lower e.g. at 80 kV they are 0.5 keV and 2.0 keV respectively. The key factors giving the improvement are an increase in the energy-loss at which the projector cross-over goes to infinity and a reduction of the combination aberrations that occur in a lens stack. As well as improving the energy-loss range, the new set-ups reduce spectrum artefacts and minimise the motion of the diffraction pattern at low STEM magnification for electrons that have lost energy. Even if making the pivot points conjugate with the film plane gives no motion for zero-loss electrons, there will be motion for those electrons that have lost energy, leading to a false sense of security when performing spectrum imaging at low magnifications. De-scanning of the probe after the objective lens is a better way of dealing with this problem.

© 2017 Elsevier B.V. All rights reserved.

1. Introduction

It is a pleasure to contribute to this Festschrift in celebration of the work of Ondrej Krivanek (OLK). He started his research career at the Cavendish Laboratory at a similar time to that at which one of the authors (AJC) started his. OLK's interest then was on conventional HRTEM whereas AJC was working with the first production VG Microscopes HB5 scanning transmission electron microscope (STEM) and its electron energy-loss spectrometer. This was in the early days of what is now known as STEM-EELS. When OLK moved to Berkeley, he became involved in developing an EELS spectrometer. This led to him to joining Gatan, where it was commercialised. While at Gatan, he was instrumental in developing a post-column energy filter and then an EELS spectrometer with parallel readout, a PEELS spectrometer. His experience of using computerised systems to set up and tune the filter led to his starting NION to apply this expertise to aberration corrected STEM.

With the HB5 at the Cavendish Laboratory, the probe angle, α, used was in the range 4 to 16 mrad, and was much bigger than the collection angle, β, which was in the range 1 to 2.5 mrad. Thus a large fraction of the available signal was lost. When AJC moved to Glasgow, the group there acquired an HB5 with three post-specimen lenses. These lenses allowed the scattering distribution leaving the specimen to be compressed into the small acceptance angle of the EELS spectrometer giving $\beta > \alpha$ and typically in the range 12.5 to 25 mrad. This gave much greater signal collection efficiency for EELS.

During the period that the PEELS spectrometer was being developed at Gatan, IBM Research Laboratories Almaden acquired an HB5 with the same optical arrangement as that in Glasgow. AJC spent a short period at Almaden helping to set-up the post-specimen optics. It was hoped that the PEELS spectrometer system would be ready to be demonstrated on this HB5 during his visit. While this did not happen as planned, the striking results subsequently obtained by Krivanek and Paterson [1,2] on the Almaden instrument made use of this post-specimen lens set-up.

This brief historical introduction leads directly onto the subject of the current paper, which is the optimisation of the post-specimen optics for STEM-EELS. Whether the STEM is a very powerful (and very expensive) dedicated STEM or a very powerful (and very expensive) TEM/STEM, the coupling between it and the

---

* Corresponding author.
E-mail address: ian.maclaren@glasgow.ac.uk (I. MacLaren).

http://dx.doi.org/10.1016/j.ultramic.2017.03.017
0304-3991/© 2017 Elsevier B.V. All rights reserved.

Please cite this article as: A.J. Craven et al., Getting the most out of a post-column EELS spectrometer on a TEM/STEM by optimising the optical coupling, Ultramicroscopy (2017), http://dx.doi.org/10.1016/j.ultramic.2017.03.017

very powerful (and very expensive) EELS system is provided by the post-specimen optics. In a TEM/STEM column, this consists of the objective lens post-field and the projector system. In a system without an image aberration corrector, a modern projector system typically consists of four lenses. In addition, there can be a “mini-lens” in the back-bore of the objective lens.

Originally, the projector system in a TEM was designed and optimised to give:

- high magnification imaging;
- an image at the selected area aperture plane;
- diffraction patterns with low radial and spiral distortion.

As the systems evolved and more lenses were added to give higher magnification, other features could be added e.g. rotation-free imaging, rotation-free diffraction. All of these features are designed for electrons that have lost no (or very little) energy.

In one area of application, the low magnification imaging of thick specimens, the effect of energy-loss was considered. Here the projector system could be set up to give zero change of magnification and zero change of rotation with energy-loss significantly improving the imaging of thick specimens at low magnifications[1] [3].

When studying energy-loss events themselves, there are two modes in which the spectrometer system can be operated, the energy filtered TEM mode (EFTEM) or the electron energy-loss spectroscopy mode (EELS).

In EFTEM, an image or diffraction pattern is present on the spectrometer entrance aperture. A spectrum is formed in the dispersion plane of the sector magnet and a slit is used to define the energy range that can pass into the subsequent multi-pole optics. This optics is used to reconstruct the image or diffraction pattern present at the entrance aperture on the spectrometer camera.

Thus, in EFTEM mode, only a relatively narrow range of energies is required to pass through the system. Moreover, the extra high tension (EHT) of the microscope is altered so that a given loss passes through the post-specimen optics and filter with the same energy as the zero-loss electrons i.e. to image electrons that have lost 1 keV of energy, the EHT is raised by 1 keV. Thus all of the careful optimisation of the post-specimen optics and the filter is preserved.

In EELS, the dispersion plane of the spectrometer is imaged onto the spectrometer camera in the form of a line image at a magnification to give a spectrum with the required dispersion. Since the spectrum contains a wide range of energy-losses, all these electrons must pass through the system at the same time, irrespective of their energy-loss. The greater the energy-loss, the stronger each optical element becomes. Thus the change in the properties of the post-specimen optics must be considered.

When used in the normal STEM-EELS mode, there is a diffraction pattern on the spectrometer aperture. This is termed image coupling by Egerton [4] since the object for the spectrum is an image of the specimen. In this mode, the chromatic effects in the optics resulting from energy-loss include:

- change of camera length;
- change of the axial position of the final cross-over of the projector system, which is referred to as the PL cross-over below;
- change of the radial and spiral distortion of the diffraction pattern;
- change in the projector system alignment.

Each of these effects can result in a change of the collection angle with energy-loss, with a corresponding effect on the partial differential cross-section required for quantification. This will affect the result of quantification when using theoretical differential cross-sections in the normal way i.e. where the collection angle is assumed to be independent of energy-loss and equal to that measured for zero-loss electrons.

It is now possible to measure accurate experimental differential cross-sections [5,6]. Provided the data they are used to quantify are taken on the same instrument under the same conditions, the chromatic effects cancel out. However, to use them on a different instrument, or to compare them to theoretical cross-sections calculated in the way outlined above, then it is important to understand and minimise the change of collection angle with energy-loss.

Craven and Buggy [7] analyse such chromatic effects in a VG HB5 dedicated STEM with post-specimen lenses. Several authors [8–10] analyse the effects of energy-loss in the projector lenses of a CTEM but concentrate on their effect on the energy resolution. Titchmarsh and Malis [11] consider the effects on collection efficiency for a CTEM column but assume that the aberrations of the intermediate lenses play no role. Yang and Egerton [12] find that the intermediate lenses dominate the effects in a CTEM column. All of this early work on CTEM projector systems is for camera lengths an order of magnitude greater than those required to accept the probe angles used in instruments equipped with probe correctors. At these shorter camera lengths, the effects are much more severe. This paper investigates these effects in detail.

A given camera length can be obtained with more than one set-up of the projector system. The resulting chromatic behaviour will depend on the particular set-up and this depends on how the individual lenses behave. If a lens forms a real image and the next lens is beyond this image, the image acts as a real object for that next lens. Here the first lens is said to be in Mode R. However, if the next lens is before the image position of the first lens, then the image acts as a virtual object for the next lens. The first lens is said to be in Mode V. If the first lens forms a virtual image, this virtual image acts as a real object for the next lens and the first lens is said to be in Mode V’.

If all lenses in the projector system are in Mode R, the camera length increases with increasing energy-loss as seen in Mode II of the Craven and Buggy paper [7]. (In that paper, the effects are described in terms of the *angular compression* of the projector system, which is inversely proportional to the camera length). However, if the projector lenses have some V and/or some V’ modes, it is possible to make the camera length decrease with energy-loss as seen in Mode I of Craven and Buggy [7]. The reason for this is that, as the lens in the V or V’ mode increases in strength because of the energy-loss, the rays move closer to the axis in the subsequent lens. Thus they are less strongly focussed by the subsequent lens even though it has become stronger.

These calculations also show that, at one camera length in Mode I, the change of camera length with energy-loss is zero to first order. That this occurs is not surprising since it is the equivalent of achieving zero change of magnification with energy-loss in imaging. The reason that there is only one camera length at which this occurs in their setup is that it only has two degrees of freedom. Designing the projector system so that there is a fixed final cross-over position adds one constraint, allowing a range of camera lengths to be obtained. Requiring the camera length to be independent of energy-loss adds a second constraint, which means that this can only be achieved at a single camera length.

This leaves no degrees of freedom to achieve other desirable features such as:

- a range of camera lengths which are independent of energy-loss;
- zero radial distortion for zero-loss electrons;
- zero radial distortion independent of energy-loss;

---

[1] One of the authors (AJC) heard that the Philips EM400 had a lens series with these properties in a talk given by Philips in about 1979.

- imaging the STEM pivot points to the spectrometer aperture so that the diffraction pattern does not scan at low STEM magnification for zero-loss electrons;
- imaging the pivot points to the aperture independent of energy-loss;
- minimising the change in the power dissipated in the projector system when the camera length is changed.

Even with the extra two degrees of freedom provided by the four lenses in the projector system of a modern TEM/STEM, there are not enough degrees of freedom to achieve all of these features and so the best compromises must be sought.

Below, the performance of the projector system of a commercial, high performance TEM/STEM equipped with an EELS system is compared for different set-ups. The specimen height and the objective lens excitation are kept constant so that the probe forming optics is unchanged. The specimen is conjugate with the selected area diffraction (SAD) aperture plane. Thus, only the excitations of projector system lenses are changed.

2. Experimental methods

The system under investigation is a JEOL ARM 200CF fitted with a probe corrector, a cold field emission gun and a Gatan 965 Quantum ER spectroscopy system. The Quantum is equipped with fast DualEELS and spectrum imaging [13,14].

For the work in this paper, the system is operated at 200 kV. The probe half angle, α, is 29 mrad, giving sub-Ångström resolution. To give good collection efficiency for EELS, the spectrometer must have a collection half angle, β, which is greater than α. The value of β is 36 mrad when using the 2.5 mm spectrometer aperture and this is given by a camera length of approximately 2 cm at the film plane.

In line with JEOL notation, the first three of the four lenses in the projector system are called intermediate lenses (IL1, IL2 and IL3) while the final one is called the projector lens (PL). There is an aperture immediately after the PL (the PL aperture). This aperture has a small diameter and separates the poorer vacuum in the detector chamber from the better vacuum in the column liner tube. To avoid this aperture limiting the field of view, all the TEM magnification modes and normal camera lengths have the PL cross-over in (or very close to) the plane of the PL aperture.

The Quantum is set-up to use this PL aperture plane as its object plane. However, as will be seen below, it is necessary for the PL cross-over to move out of the PL aperture plane to achieve the short camera lengths required for STEM-EELS. The quadrupoles preceding the magnetic sector of the spectrometer are then used to refocus the spectrum.

In STEM-EELS, there is a diffraction pattern on the Quantum entrance aperture. To investigate the influence of the projector set-up on these diffraction patterns, they are recorded on an Orius camera prior to the Quantum aperture. A Si [001] specimen is used. Patterns are taken with the specimen oriented on this pole and also tilted off it by ~23° towards [111]. The former are used to measure the camera length and estimate the 3rd order distortion. The latter can be used to investigate the distortion in more detail. Three successive exposures of each pattern are made (with exposure time increasing by a factor of 5 for each exposure) and merged together using a standard high dynamic range photography approach (similar to that of Evans and Beanland [15]). In this way, good signal to noise ratio is obtained over the whole angular range. This acquisition is performed using a custom script provided by Dr Bernhard Schaffer of Gatan GmbH (http://dmscript.tavernmaker.de/).

To see how the patterns change with energy-loss, a procedure similar to that used by Yang and Egerton [12] is adopted. The EHT of the microscope is changed using the EHT offset function provided for EFTEM. This covers a range from + 3 kV to −3 kV. Applying this offset leaves the excitations of the lenses unchanged. Thus if the EHT is lowered, the post-specimen ray paths correspond to those for electrons that have lost the corresponding amount of energy. Raising the EHT gives the ray paths for electrons that “gain” energy. While this does not happen to any significant degree in practice, it is useful for studying the properties of the projector system.

However, the pre-specimen optics is also changed so that the probe must be re-focused on the specimen using the condenser system. This causes the probe half-angle (and hence the size of the diffraction discs in the pattern) to change, the sign of the change depending on which condenser lens used. Thus, in principle, the change could be made zero by using a combination of pre-specimen lenses to refocus the probe.

Yang and Egerton [12] observe shifts in the position of the diffraction pattern with energy-loss. In principle, these shifts can also be measured here. In practice, the results prove inconclusive because there are also effects from the re-focussing of the probe and from the procedure required to do this.

To show the corresponding spectrometer behaviour, spectra are recorded from a Si specimen using the camera view mode with a dispersion of 1 eV per channel and both the 2.5 and the 5 mm Quantum apertures. The camera view mode is the 2D image of the spectrum on the UltraScan camera of the Quantum. The energy-loss is in the horizontal direction. In the vertical direction, the position is a function of the position of the ray in the entrance aperture i.e. the diffraction pattern here. The actual spectrum is given by summing the camera view over this direction. Offsets of 0.25, 1, 2 and 3 keV are used with the DualEELS system to give a camera view covering the range from −0.2 keV to 4.848 keV.

To compare the EELS performance of two of the projector set-ups in detail, DualEELS is used to record spectrum images (SIs) from the same region of a MoO_2 powder sample on a holey carbon film. The Quantum aperture is 2.5 mm. The dispersion is 0.5 eV/channel, the low loss integration time is 100μsec and the high loss integration time is 200 ms. The region covered by the SI has a range of thickness so that spectra at a number of thicknesses can be extracted and compared.

3. Ray tracing

With four projector lenses, there are very many ways of achieving a given camera length. Thus, first order ray tracing is used to identify set-ups which give:

- the same camera length as the standard microscope set-up.
- zero change of camera length with energy-loss;
- zero (or small) change of the position of the PL cross-over for zero loss electrons;
- the pivot points of the scan conjugate with the film plane[2];

The first condition ensures that future data is compatible with past data. The second condition gives no (in practice, a small) change of collection angle with energy-loss. The third condition maintains the spectrum focus. The fourth condition keeps the diffraction pattern stationary to first order on the film plane as the probe is scanned, at least for zero-loss electrons.

This process uses matrix multiplication of a series of free space propagation matrices and first order lens matrices. The propagation

---

[2] In an ideal system, this is equivalent to focusing the diffraction pattern onto the film plane. However, since the area illuminated on the specimen is so small, defocus of the pattern causes no loss of detail in the pattern since each point in it has effectively only one “ray” passing through it. Thus some relaxation of this constraint can be beneficial, as discussed later in the paper.

Please cite this article as: A.J. Craven et al., Getting the most out of a post-column EELS spectrometer on a TEM/STEM by optimising the optical coupling, Ultramicroscopy (2017), http://dx.doi.org/10.1016/j.ultramic.2017.03.017

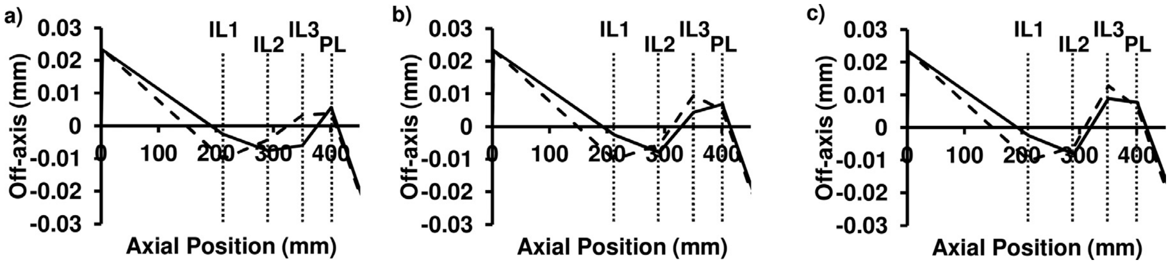

Fig. 1. The off axis positions of 1st order rays versus their axial position for zero-loss (solid line) and 1 keV loss (dashed line) electrons leaving the specimen with a slope of 10 mrad. a) Set-up A; b) Set-up B; c) Set-up C. The specimen is on axis at an axial position of zero and the ray moves rapidly off-axis in the very short distance between the object and the objective lens. For a given energy-loss, the ray paths prior to IL1 are the same in all three set-ups because the specimen position and objective lens excitation are held constant.

matrix converts the off-axis position of the ray and its slope at the start to that after a propagation distance of x (Eq. 1).

$$\begin{vmatrix} 1 & x \\ 0 & 1 \end{vmatrix} \tag{1}$$

The first order lens matrix converts these values immediately before a thin lens of focal length, f, to those immediately after it (Eq. 2).

$$\begin{vmatrix} 1 & 0 \\ -1/f & 1 \end{vmatrix} \tag{2}$$

The focal lengths are related to the lens properties and lens currents using finite element field calculations and standard electron optical integrals [16]. The lens currents are parameterised in terms of the excitation parameter $V_R/(NI)^2$ where $V_R = V[1 + (eV/2m_oc^2)]$. V is the accelerating voltage, N is the number of turns in the lens winding, I is the lens current, e is the charge on the electron, m_o is the rest mass of the electron and c is the speed of light. To make a correction for the difference between the ideal value of NI and that found in practice, the focal length of each projector lens is measured[3] and the ideal value of NI is scaled to match the experimental one. The loss rays can be traced by changing the excitation parameters of the lenses appropriately. The focal length of the objective lens (OL) is that appropriate for the CTEM mode of operation and its focal length is changed using the corresponding chromatic aberration coefficient, C_c.

For the standard 2 cm camera length provided for the ARM, called Set-up A below, Fig. 1a shows the 1st order ray paths for zero-loss electrons (solid line) and for 1 keV loss electrons (dashed line). The rays leave the specimen on axis with a slope of 10 mrad and so they move rapidly off-axis before being bent back towards the axis by the strong objective lens. This section of the trajectory between the object and the objective lens is not clear in Fig. 1 due to the short distance between them. In Set-up A, the PL cross-over is ~8 mm beyond the PL aperture. Table 1 analyses the lenses in terms of the lens modes introduced above (R, real image formed before the next lens, V, real image formed after the next lens, V', virtual image). It is interesting to note that the configuration for IL1, IL2 and IL3 (i.e. V' VR) in Set-up A is the same as that in Mode I of the paper by Craven and Buggy [7].

The loss of 1 keV of energy makes a large difference to the ray paths and modifies the lens modes but has little effect on the final slope. This means that the camera length is independent of energy-loss to a good approximation over this energy range.

Table 1
Lens modes for Set-ups A, B and C.

Set-up	Loss (keV)	OL	IL1	IL2	IL3	PL
A	0	R	V'	V	R	R
	1	R	V	R	V'	R
B	0	R	V'	R	V'	R
	1	R	V	R	V	R
C	0	R	V'	R	V	R
	1	R	V	R	V	R

However, at larger energy-losses, there is a significant change in the camera length with energy-loss and this causes a corresponding change in the collection angle for EELS. As will be seen below, there are also issues with the cut-off of the diffraction pattern and the corresponding behaviour of the spectrum in the camera view.

The most promising sets of lens values identified by the search process are then investigated in the ARM and each optimised to give the best performance. The set-ups that give the best performance in practice have their performance measured in detail. Two are considered here. The lens values in Set-up B have been chosen to image the pivot points to the plane of the film camera while those in Set-up C have been chosen with this constraint relaxed slightly. Figs. 1b and c show the equivalent ray paths for Set-ups B and C respectively and Table 1 gives the lens configurations.

To understand the behaviour fully, the chromatic aberration and the spherical aberration have to be included in the ray tracing. For the OL, the spherical aberration coefficient, C_s, and chromatic aberration coefficient, C_c, are known for its standard excitation. Since the projector lenses are relatively weakly excited, thin lens approximations work well. From Haine and Cosslett [17], C_c can be taken as equal to f while C_s is related to f and the sum of the gap, S, and the bore diameter, D, of the lens by

$$\frac{C_s}{f} = \frac{5f^2}{(S+D)^2} \tag{3}$$

For stronger lenses, C_c becomes smaller and C_s becomes larger than these approximations.

The chromatic aberration means that f becomes $f' = (f - C_c \Delta V_R / V_R)$. Spherical aberration means that f' is a function of the distance off-axis, r, at which a ray passes through the lens. Thus f' becomes $(f' - C_s r^2 / f'^2)$ where C_s is appropriate for the value of f'. These values can be put into Eq. 2 and used to trace the rays for different slopes of the ray at the specimen and different energy-losses.

Fig. 2 shows the zero-loss rays in Set-up A that leave the specimen on-axis with slopes in 20 mrad increments. The right hand side of the figure represents the diffraction pattern. The dashed rays are those that leave the specimen with a slope of less than

---

[3] The method of measuring the focal length of a projector lens makes use of the fact that, if the lens of interest focuses a point image into the centre of a subsequent, thin lens, the second lens has no effect on the paraxial rays whatever its strength. Thus adjusting the strength of the first lens until variation of the strength of the second lens makes no difference to the final image identifies the image plane of the first lens as the position of the second lens. Combining this with the position of the object plane (e.g. the selected aperture plane, if this is conjugate with the specimen) allows the focal length of the first lens to be found.

Please cite this article as: A.J. Craven et al., Getting the most out of a post-column EELS spectrometer on a TEM/STEM by optimising the optical coupling, Ultramicroscopy (2017), http://dx.doi.org/10.1016/j.ultramic.2017.03.017

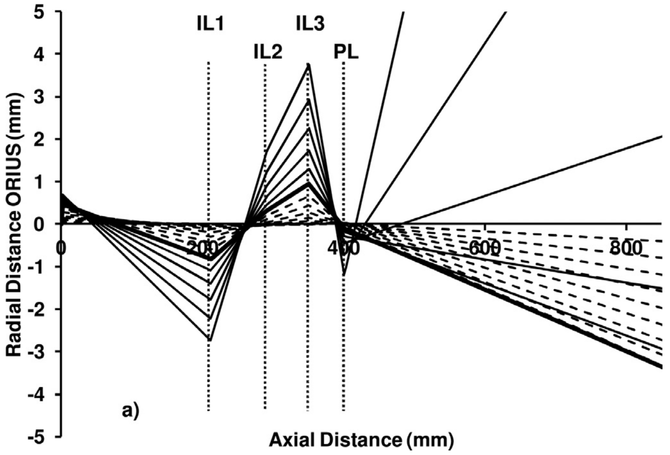

Fig. 2. Rays traces for zero-loss electrons leaving the specimen on-axis with slopes in increments of 20 mrad when using Set-up A. As the slope of the ray at the specimen increases, the dashed rays increase their downward distance from the axis after the PL. The thick black ray leaves the specimen with a slope of 200 mrad and has the greatest downward distance from the axis after the PL. Thus it forms the cut-off of the diffraction pattern if it is not intercepted by the PL aperture. The thin solid black rays leaving the specimen with slopes greater than 200 mrad are folded back inside the cut-off after the PL and some eventually re-cross the axis.

200 mrad. After the PL, these rays increase their distance from the axis in the downward direction as their initial slope increases. Thus, in the diffraction pattern, their distance from the axis increases with slope, as expected. However, as the slope approaches 200 mrad, the aberrations cause the separation of the rays to decrease. The ray leaving the specimen with a slope of 200 mrad (the thick black ray) is the one that arrives at the diffraction pattern at the maximum downward distance from the axis. Thus it will form the cut-off of the diffraction pattern provided that it is not intercepted by the PL aperture (see below). The thin solid rays are those leaving the specimen with slopes higher than 200 mrad and these are folded back towards the axis after the PL and the rays with highest angles eventually re-cross the axis. As will be seen below, all three of the set-ups show similar behaviour but the actual slopes and the effect of the PL aperture differ from set-up to set-up.

4. Results and discussion

4.1. Camera views and diffraction patterns

Fig. 3 shows a montage of the camera views for the three set ups. They are recorded in 2.048 keV sections with offsets of 0, 0.25, 1, 2 and 3 keV. Also shown in Fig. 3 are diffraction patterns recorded with EHT offset using 0.5 keV steps. A smoothing filter and a Laplacian filter are applied to the patterns so that the whole angular range is visible. No angular calibration is provided as both the camera length and the distortion change through the series, which is the key message. The circles on the diffraction patterns represent the 5 mm Quantum aperture and its diameter corresponds to 144 mrad for zero-loss electrons. The vertical dashed lines provide the energy scale for the camera views and also identify the energy-loss of each diffraction pattern. Larger versions of some of the diffraction patterns are provided in Figure S1 in the supplementary material.

In the camera view, there are real features: the zero-loss peak (ZLP), the plasmon peaks (not labelled), the Si L-edges, the Si K-edge and the peak from the stray electrons that are generated by the first anode in the gun (A1).[4] In addition, there are discontinuities where two sections of the camera view are joined i.e. at 0.8, 2.8 and 3.8 keV. For example there is a discontinuity in intensity at 2.8 keV and this is required because of the change of intensity with energy loss. However, there is also a discontinuity in the width in the vertical direction. Such a discontinuity cannot be caused by the projector system since the change in width is observed at the same energy-loss. Such discontinuities are the result of chromatic effects in the Quantum system itself, which cause the intensity band to narrow across the field of view. This narrowing is clearly seen in the range from 0.8 to 2.8 keV. However, as the offset changes, the width at a particular position in the field of view decreases only very slowly (see Figure S2 in the supplementary material). Thus, at 2.8 keV in Fig. 3, where the right hand edge of the camera view with an offset of 1 keV is joined to the left edge of a camera view with an offset of 3 keV, a discontinuity in width occurs. The reasons for such chromatic effects in the spectrometer are not considered in this paper.

It is clear that the diameter of the cut-off of the diffraction pattern decreases with energy-loss in all three set-ups and that this diameter is smallest for Set-up A and largest for Set-up C at a given energy-loss. As the energy-loss increases, the diameter of the pattern becomes comparable with that of the 5 mm Quantum aperture, as in the case of the pattern for a 3 keV loss in Fig. 3a (Set-up A). At even higher energy-loss, the pattern falls entirely inside the aperture.

4.2. The change of camera length with energy-loss

The experimental camera lengths are obtained by measuring the separations of the (400), (040), (440) and (4$\bar{4}$0) Kikuchi lines close to the centre of the diffraction patterns taken with the specimen oriented on the [001] pole. NB the change in the size of the central disc with energy-loss is not related to the change of camera length but is the result of re-focusing the probe with the condenser mini-lens.

The equivalent camera lengths on the Orius camera can be obtained from the ray tracing by setting C_s to zero. The lens strengths used in the ray tracing are adjusted so that the camera lengths obtained match the experimental ones over the experimental energy-loss range. These lens strengths are used for all subsequent results in this paper.

The results are shown in Fig. 4. For all three set-ups, the camera length goes through a maximum at some energy-loss. The curvature of the data decreases on going from Set-up A to Set-up B to Set-up C. Thus, with Set-ups A and B, the camera length is a maximum at zero-loss but the change of energy loss required to cause a given decrease in camera length is bigger for Set-up B than for Set-up A. However, for Set-up C, the camera length initially increases with energy loss and only starts to fall for energy losses greater than ~2.2 keV.

Even though Set-up B has greater curvature than Set-up C, the fact that the maximum occurs at zero-loss means that it gives a nearly constant camera length out to 1 keV. On the other hand, Set-up C gives a slightly smaller camera length at zero-loss while giving a very constant camera length over the energy range from 1

---

[4] Whenever electrons hit the edge of an aperture, they generate secondary electrons with very low energy. If the aperture is within the accelerating structure, these secondary electrons are accelerated down the column. Their energy is lower than the majority of the electrons by an amount corresponding to the difference in the potential of the emitter and the aperture. Thus they appear as a loss peak in the EELS spectrum. With the JEOL cold field emission gun, peaks from the first and/or second anodes may be seen, depending on the particular settings of the gun. Their source can be verified by comparing the energies of the peaks with the voltages on the electrodes.

Please cite this article as: A.J. Craven et al., Getting the most out of a post-column EELS spectrometer on a TEM/STEM by optimising the optical coupling, Ultramicroscopy (2017), http://dx.doi.org/10.1016/j.ultramic.2017.03.017

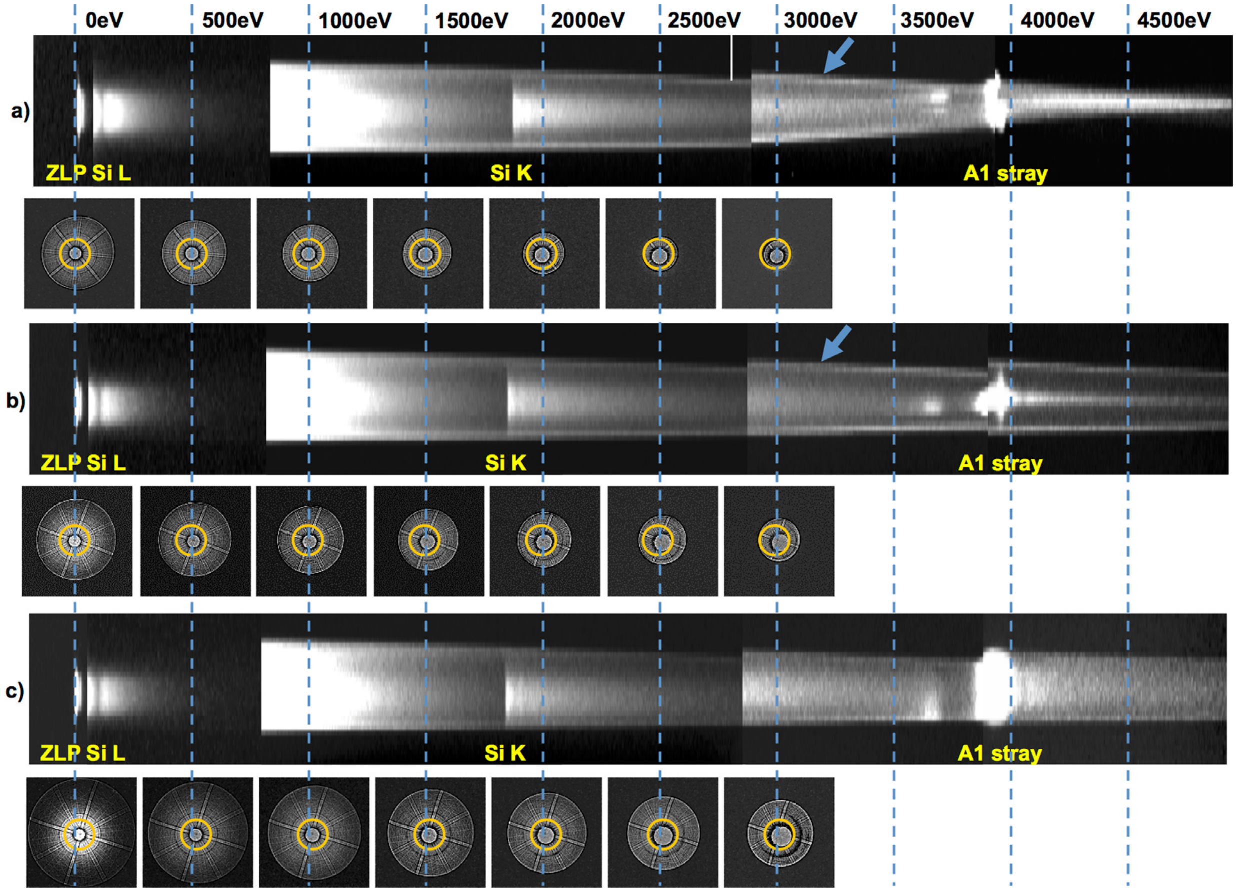

Fig. 3. Montages of camera views recorded with the 5 mm Quantum aperture and associated diffraction patterns corresponding to a set of energy-losses at 0.5 keV intervals. a) Set-up A; b) Set-up B; c) Set-up C. The vertical dashed lines provide the energy scale for the camera views and identify the energy-loss of the diffraction patterns. The circles on the diffraction patterns correspond to the diameter of the 5 mm Quantum aperture, which corresponds to 144 mrad for zero-loss electrons. The arrows point to examples of the bright edge caused by the fold-back of the diffraction pattern in Setups A and B. A smoothing filter and a Laplacian filter are applied to patterns so that the whole angular range is visible. Larger versions of the patterns are given in Figure S1 in the supplementary material. N.B. The increase in the size of the central disc is due to the change of the excitation of the condenser mini-lens when re-focusing the probe and not indicative of the change of camera length.

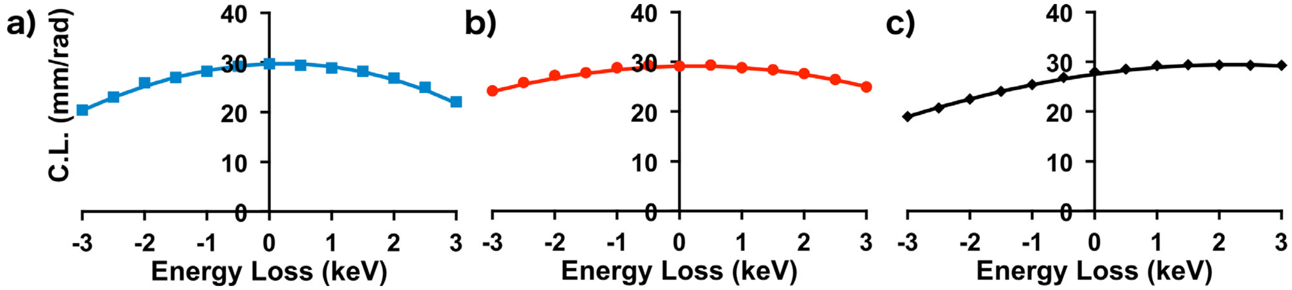

Fig. 4. Comparison of camera lengths on the Orius camera from experiment (points) and from ray tracing (lines) as a function of energy-loss. a) Set-up A; b) Set-up B; c) Set-up C. The lens strengths in the ray tracing have been adjusted to give agreement between the experimental and traced values.

to 3 keV, making it suitable for use at higher energy-losses. However, in this case, the collection angle measured at zero-loss will have to be corrected to that applicable in the 1 to 3 keV range for the most accurate work. Thus the choice of which set-up to use will depend on the specific system being investigated. It is possible to shift the energy-loss at which the maximum of the camera length occurs and so the set-up can be further tailored to meet the experimental requirements.

4.3. The maximum diameter of the diffraction pattern and its variation with energy-loss

The cut-off diameter seen on the Orius camera is determined by two competing effects. Fig. 2 shows that, in the absence of a PL aperture, aberrations determine the slope of the ray for which the cut-off diameter of the diffraction pattern occurs. However, the presence of the PL aperture will set the maximum slope of a ray leaving the specimen that can reach the Orius camera. This may be larger or smaller than the limiting slope set by the aberrations. In the former case, the aberrations will set the cut-off and in the latter case it will be the PL aperture. Fig. 5 shows the limiting slopes from these two effects as functions of energy-loss. The solid line

Please cite this article as: A.J. Craven et al., Getting the most out of a post-column EELS spectrometer on a TEM/STEM by optimising the optical coupling, Ultramicroscopy (2017), http://dx.doi.org/10.1016/j.ultramic.2017.03.017

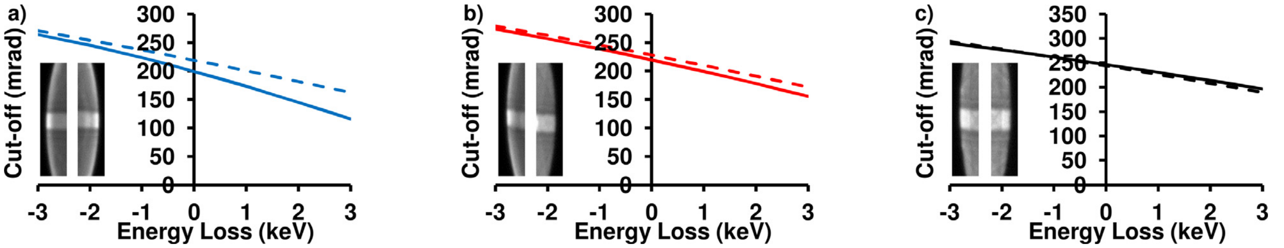

Fig. 5. Cut-off ray slopes at the specimen from aberration (solid lines) and the PL aperture (dashed lines) versus energy-loss. a) Set-up A; b) Set-up B; c) Set-up C. The left and right hand edges of the corresponding zero-loss diffraction patterns on the Orius camera are shown inset. Where the solid line is below the dashed line, the edges of the pattern should have a bright edge resulting from the fold-back.

is the limit set by aberration and the dashed line that set by the PL aperture. Where the solid line is below the dashed line the pattern folds back at the edge. If the solid line is above the dashed line, the PL aperture prevents such fold-back.

Fig. 5a predicts significant fold-back for Set-up A. The left and right hand edges of the on-pole, zero-loss diffraction pattern are shown inset. The bright edges show that fold-back is present. Fig 5b predicts a small amount of fold-back in Set-up B. The left hand edge in the inset shows fold-back but the right hand side does not and this is presumably the result of a slight misalignment of the projector system. Fig. 5c predicts no fold-back over the energy-loss range from −1 to 3 keV in Set-up C. Its absence at zero-loss is confirmed by the inset.

When fold-back is present in the diffraction pattern, it should also show up in the camera view of the spectrum when the size of the diffraction pattern approaches and becomes smaller than that of the 5 mm Quantum aperture. Fig. 3a and b do show bright top and bottom edges to the intensity band e.g. those at the top are indicated by arrows. However, these bright edges extend to lower energy-losses, where the diffraction patterns are significantly larger than the 5 mm Quantum aperture. Thus they must be caused by aberration effects within the spectrometer itself. However, in Fig. 3a, these bright bands become stronger for losses of 3 keV or greater and this is confirmed by vertical line profiles through the band (see Figure S3 in the supplementary material). This increase in the edge intensity is due to the whole pattern, with its fold-back, entering the 5 mm aperture. A similar effect can be seen at higher energy-losses in Fig. 5b but is absent in Fig. 5c.

The cut-off slopes in Fig. 5 allow the positions of the cut-off diameters on the Orius camera to be predicted. The corresponding experimental diameters in pixels are obtained by fitting circles to the edges of the diffraction pattern and these are converted to mm using the 9μm pixel size of the Orius camera. The results from experiment and ray tracing are shown in Fig. 6. The agreement is very good and the experimental behaviour with energy-loss is well reproduced by the ray tracing.

4.4. *Radial distortion in the diffraction pattern and its variation with energy-loss*

The cut-off of the diffraction pattern by the aberrations is the result of radial distortion in the pattern. This can be analysed in more detail by examining the positions on the Orius camera of the rays with different initial slopes at the specimen. The radial distortion is the difference in the position of the actual ray and that predicted by the first order camera length. For a single round lens with only third order aberrations, the radial distortion is third order. However, in a stack of such lenses, each with third order aberrations, combination aberrations cause distortions with higher order odd powers.

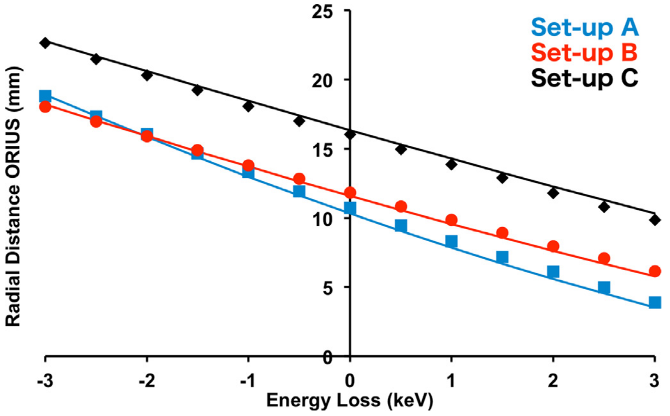

Fig. 6. Comparison of the diffraction pattern cut-off diameters versus energy-loss for the three set-ups. The experimental diameters are shown as points and those from ray tracing as lines. The labels show the set-ups.

Fig. 7 shows the distances of the rays from the centre of the zero-loss diffraction patterns on the Orius camera as functions of their slopes at the specimen. The vertical dotted lines are the maximum slopes that will pass through the PL aperture. Plots for other energy losses are given in Figure S4 of the supplementary material.

To fit the distortions obtained from the ray tracing, 3rd· 5th, 7th and 9th order distortions must be included. The contributions of the various orders of distortion are shown as a stacked series of dashed plots i.e. the line with the label “1” is the contribution of the linear camera length while that with the label “1,3” is the combination of the camera length and the 3rd order distortion and so on. The curve with the label “1, 3, 5, 7, 9” is the total fit and lies over the black line for the actual positions, giving a light blue/black dashed line. It can be seen from the plots that the 3rd and 7th order distortions are positive while the 5th and 9th order distortions are negative. In Fig. 7a and b, the position follows the linear camera length up to relatively high slopes and then drops below it indicating low radial distortion in the centre of the pattern and negative radial distortion as the edge is approached. Thus, for Set-ups A and B, there appears to be a correlation between the energy at which the central radial distortion is low and that at which the maximum camera length occurs.

In Fig. 7c (Set-up C), the position initially rises above the linear camera length before dropping below it at higher slopes indicating positive radial distortion in the centre of the pattern turning to negative radial distortion as the edge is approached.

Fig. 8 shows the zero-loss diffraction tilted off the [001] pole by $\sim$23° towards [111] and is recorded using Set-up C. The pattern has had a smoothing and a Laplacian filter applied. The scale of the pattern is given by the $2\bar{2}0$ Kikuchi band running through the zero disc. Its width is 13 mrad. In the central region of the pattern, the Kikuchi lines curve away from the centre of the pattern showing positive radial distortion but, as the edge of the pattern is approached, the curvature gradually changes sign showing that

Please cite this article as: A.J. Craven et al., Getting the most out of a post-column EELS spectrometer on a TEM/STEM by optimising the optical coupling, Ultramicroscopy (2017), http://dx.doi.org/10.1016/j.ultramic.2017.03.017

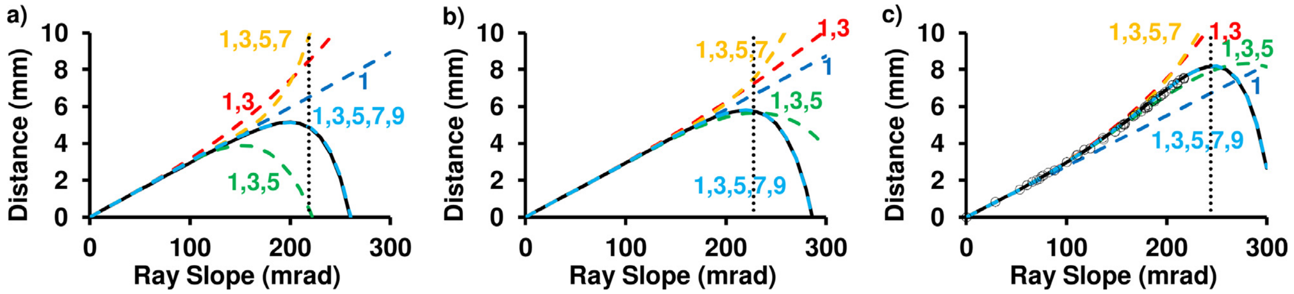

Fig. 7. Plots of the distance of a ray from the centre of the diffraction pattern versus its slope at the specimen (black dashed line). The other dashed lines show the contributions of distortions of various orders as a stacked set i.e. 1 corresponds to the linear camera length; 1,3 is the combination of the effect of the linear camera length and the 3rd order distortion and so on. The vertical dotted line the limit set by the PL aperture. a) Set-up A; b) Set-up B; c) Set-up C. The circles in c) are experimental measurements from the diffraction pattern in Fig. 8.

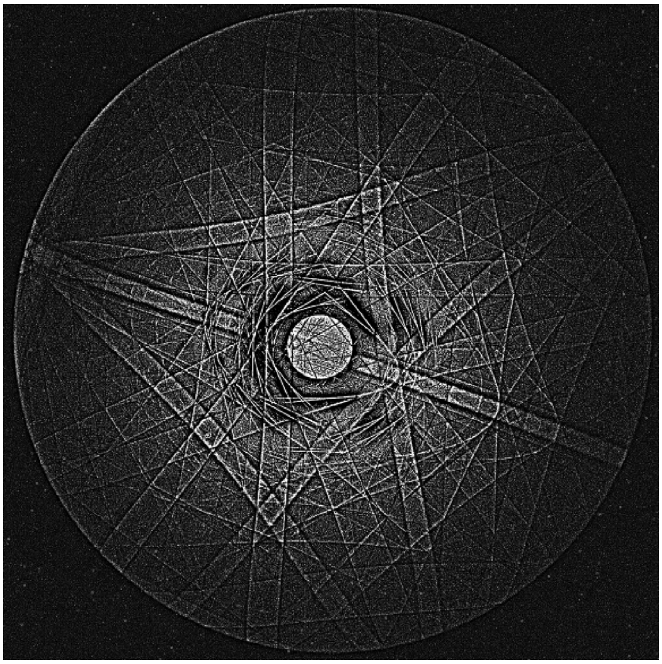

Fig. 8. Zero-loss diffraction pattern with the sample tilted off the [001] pole by ~23° towards [111] obtained using Set-up C. A smoothing and a Laplacian filter are applied. The field of view is 1800 pixels (16.2 mm) wide on the Orius camera. The scale of the pattern is given by the $2\bar{2}0$ Kikuchi band running through the zero disc. Its width is 13 mrad.

negative radial distortion is starting to dominate in agreement with Fig. 7c. Patterns recorded at other energy-losses and for the other set-ups are shown in Figure S5 in the supplementary material and show agreement with the predictions in Figure S4. Figure S4 in the supplementary material also shows Set-up C has zero radial distortion in the central zone for an energy-loss slightly greater than 1.5 keV, which is close to the energy of the maximum in the camera length in Fig. 4c. Thus the correlation between low distortion and maximum camera length is also present in this set-up.

In Fig. 8, each of the minor poles in the pattern can be indexed. This allows both their distances from the pattern centre and the true slopes of the corresponding rays to be found. These are plotted as open circles on Fig. 7c and closely follow the predictions of the ray tracing. As the edge of the pattern is approached, it becomes progressively more difficult to measure the true position of the pole. This is because the shape formed by the four intersecting Kikuchi lines becomes distorted and it is not possible to determine its centre accurately. As a result, it is not possible to determine the contribution of the higher order distortions accurately. In principle, this might be overcome by determining the angular positions of the intersections of the individual Kikuchi lines but this is not attempted.

Measuring the positions of the minor poles in this way is time consuming but still does not allow the higher order distortion coefficients to be determined. Inspection of the curves in Fig. 7 shows that 3rd order distortion dominates out to beyond 96.1 mrad, the radius of the first order Laue zone (FOLZ) for the [001] Si orientation at 200 kV. Thus a much simpler method of estimating the 3rd order distortion coefficient is adopted here. This assumes that the distortion at the FOLZ is purely 3rd order and calculates the magnitude of the distortion by the difference of the actual position of the FOLZ from its position predicted by the camera length. This is then converted to a 3rd order distortion coefficient by dividing by the cube of the true slope in radians. This procedure can be applied to both the experimental diffraction patterns and to a ray traced with an initial slope equal to that of the radius of the FOLZ.

Fig. 9 shows plots of the 3rd order distortion coefficient versus energy-loss. The solid lines are the 3rd order distortion coefficients from the fit of 3rd, 5th, 7th and 9th order terms. All cover a similar range of magnitudes. The points are the result of applying the FOLZ method to the experimental patterns and the dashed lines are the result of applying the FOLZ method to the ray tracing.

For all three set-ups there is reasonable agreement between the results from experiment and ray tracing using the FOLZ method. However, the best agreement is for Set-up C. This can be understood from Fig. 7c, where it can be seen that the “1, 3, 5, 7” curve virtually overlies the “1,3” curve, showing that the 5th and 7th order distortions cancel each other to a good approximation. Thus the pattern is well represented by 3rd order distortion until the cut-off is approached. Figure S4 in the supplementary material shows, this cancellation becomes less good as the energy-loss increases but keeps the 3rd order distortion dominant out to the FOLZ.

In all cases, with increasing energy-loss, there is an increasing divergence between the actual 3rd order coefficient and those estimated using the FOLZ method, showing that higher order terms are playing a significant role. The divergence is greatest in Fig. 9a (Set-up A) and smallest is Fig. 9b (Set-up B).

This behaviour can be understood from the comparison of the higher order coefficients in Fig. 10. In Set-up A, the magnitudes of all the higher order coefficients are much larger than in the other two set ups. Those in Set-ups B and C are much smaller but increase in the region where the actual 3rd order coefficients diverge from those obtained with the FOLZ method. Moreover, the magnitudes of the higher order coefficients increase more rapidly for Set-up C and this is paralleled by the more rapid divergence of the 3rd order coefficients in Fig. 9c for this set-up. Thus the reduction

Please cite this article as: A.J. Craven et al., Getting the most out of a post-column EELS spectrometer on a TEM/STEM by optimising the optical coupling, Ultramicroscopy (2017), http://dx.doi.org/10.1016/j.ultramic.2017.03.017

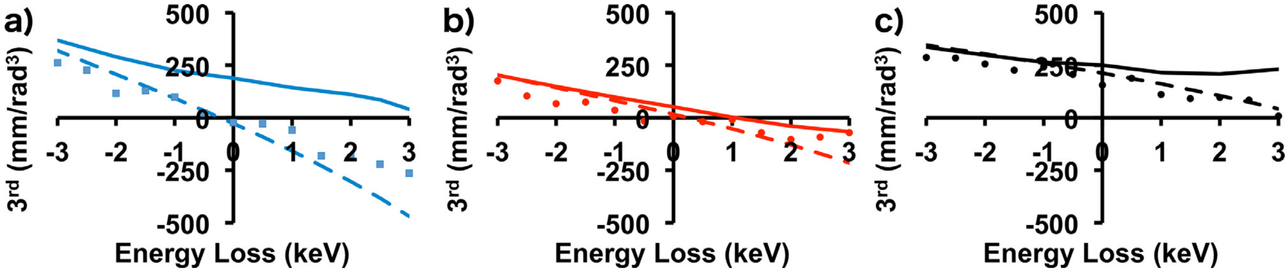

Fig. 9. Plots of 3rd order distortion coefficient versus energy-loss. The solid lines are from the fit of 3rd, 5th, 7th and 9th order terms. The points are the result of applying the FOLZ method (see text) to the experimental patterns and the dashed lines are the result of applying the FOLZ method to the ray tracing. a) Set-up A; b) Set-up B; c) Set-up C.

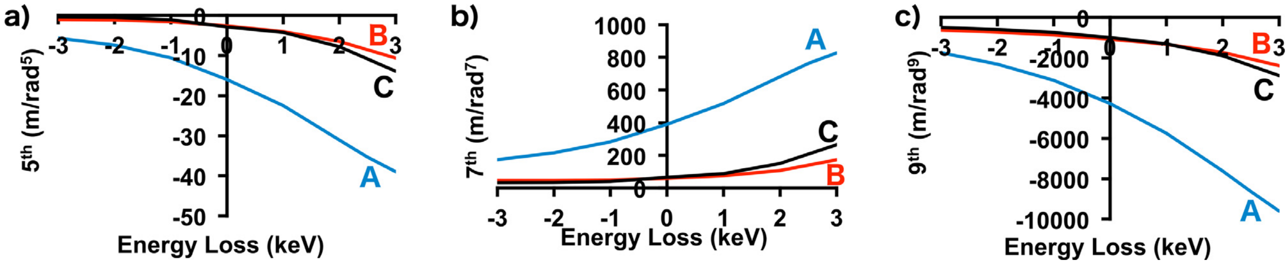

Fig. 10. Comparison of the 5th, 7th and 9th order distortion coefficients from the fits of 3rd, 5th, 7th and 9th order terms as functions of energy-loss. The labels indicate the set-ups.

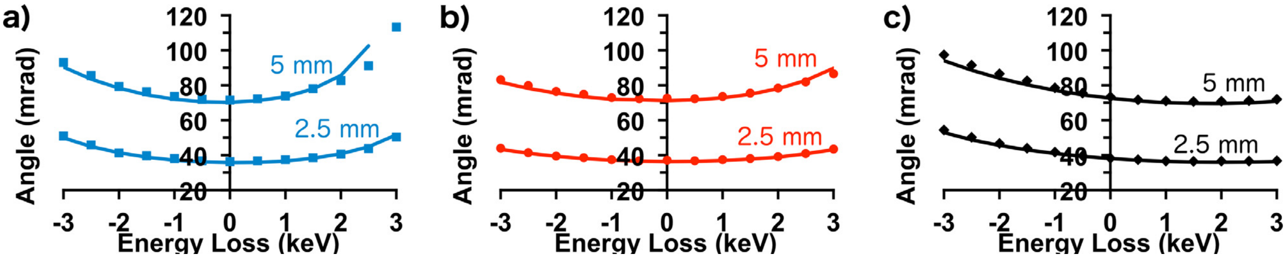

Fig. 11. Spectrometer collection half angles as a function of energy-loss predicted from ray tracing (solid line) and from the experimental diffraction patterns (points). a) Set-up A; b) Set-up B; c) Set-up C.

of the higher order distortion resulting from combination effects is a significant factor in the improved performance of Set-ups B and C.

4.5. Collection half-angles as a function of energy-loss

There is no way to image the Quantum apertures on the Orius camera because they are below it in the column. However, the corresponding diameters on the Orius camera can be calculated from the positions of the Quantum aperture plane and the Orius camera plane relative to the PL cross-over. This approach can be verified by recording the same diffraction pattern on both the Orius camera and the UltraScan camera of the Quantum. The latter can image the Quantum apertures on the same diffraction pattern so that they can then be referred to the Orius. Both approaches are in excellent agreement.

The angles to which these diameters correspond can be found from the experimental camera length and the 3rd order distortion coefficient determined using the FOLZ method. The resulting values give the experimental collection half-angles for the 2.5 mm and 5 mm Quantum apertures.

Fig. 11 plots these half-angles as a function of energy-loss as points. The predictions of the ray tracing are shown as lines. These lines give the values of the slopes of the rays at the specimen for which the rays are just intercepted by the Quantum apertures.

The agreement is very good for the 2.5 mm Quantum in all three set-ups. For Set-ups B and C, the agreement for the 5 mm aperture is good near the minimum but starts to diverge slightly away from the minimum. This divergence is more severe for Set-up A for positive energy-losses. In fact, ray tracing for a 3 keV loss gives no solution for a ray intercepting the 5 mm aperture for this set-up. The reason for this will be considered further below. The divergence between the two predictions for the 5 mm Quantum aperture is the effect of the higher order distortions discussed above as these are included in the results from the ray tracing but not in those from the experimental diffraction patterns.

4.6. The effects of the lens Set-up on the experimental Mo $L_{2,3}$-edges and Si K-edge

To show how the EELS performance differs with projector set-up in practice, six normalised spectra of the Mo $L_{2,3}$-edge are compared in Fig. 12. Three are recorded using Set-up A and three using Set-up C. All are recorded using a 2.5 mm Quantum aperture. In each group of three spectra, each spectrum has a different value of the thickness divided by the inelastic mean free path (t/λ). These values are 0.5, 1.0 and 1.5. The value of t/λ is determined from the low loss region of the spectrum. The background is subtracted using a power law fitted in a 600 eV wide window prior to the edge. The background fits for all six spectra are excellent.

Please cite this article as: A.J. Craven et al., Getting the most out of a post-column EELS spectrometer on a TEM/STEM by optimising the optical coupling, Ultramicroscopy (2017), http://dx.doi.org/10.1016/j.ultramic.2017.03.017

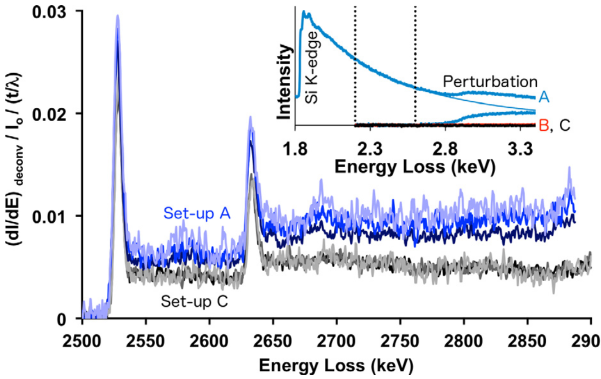

Fig. 12. Plots of the background subtracted, deconvoluted Mo $L_{2,3}$-edge intensity normalised by the zero-loss intensity, I_o, and t/λ. The upper (blue) spectra are for Set-up A and the lower (black and grey) ones are for Set-up C. The light blue and light grey spectra correspond to t/λ of 1.5, the medium blue and dark grey spectra to t/λ of 1.0 and the dark blue and black spectra t/λ of 0.5. Inset is the Si K-edge recorded using Set-up A and the 2.5 mm Quantum aperture. The background, fitted in the 400 eV window indicated by the dotted lines, is shown as a thin blue line. Also shown are the two background subtracted signals obtained when using Set-ups B (red) and C (black). The upper limit of the background subtraction window corresponds to the upper limit of that used for the Mo $L_{2,3}$-edges. (For interpretation of the references to colour in this figure legend, the reader is referred to the web version of this article.)

The single scattered intensity is obtained using Fourier ratio deconvolution of the low loss shape. The deconvoluted spectra are normalised by the zero-loss intensity, I_o, and by t/λ. Such a normalised spectrum is equal to $[n\ \lambda\ (d\sigma/dE)]$ where n is the number of Mo atoms per unit volume and $(d\sigma/dE)$ is the partial differential cross-section for the edge. n and λ are the same for all six spectra and $(d\sigma/dE)$ is the same if the probe and collection half-angles are the same. If this is the case, then all six spectra should overlie each other.

While the probe half-angle is the same for all six edges, Fig. 11 shows that the collection angle for a loss of 2.5 keV is 44 mrad in Set-up A but only 37 mrad in Set-up C. Thus the three spectra from each set-up should overlie each other but those from Set-up A should be slightly more intense than those from Set-up C.

Fig. 12 shows that the three spectra from Set-up C overlie each other so closely that it is hard to tell that there are three spectra present. Those from Set-up A are more intense, as predicted, but they do not overlie each other and their intensity continues to rise with energy-loss.

A similar effect can be seen in the inset to Fig. 12, which shows a spectrum from Si recorded using Set-up A and a 2.5 mm Quantum aperture. The power law background, fitted over the window from 2.2 keV to 2.6 keV, and the background subtracted signal are also shown. Immediately after the window, the background subtracted signal starts to rise slowly, then rises steeply in the region of 2.9 keV and then continues to rise slowly. For comparison, the background subtracted signals from spectra recorded using Set-up B (red) and C (black) are shown. These show no increase in signal after the end of the background window.

The cause of these perturbations in Set-up A is the fold-back that results from aberrations. As the bright edge of the intensity band intersects and then falls within the 2.5 mm Quantum aperture, the intensity in the spectrum is enhanced, giving rise to the perturbation. In the energy ranges shown in Fig. 12, this happens with Set-up A but not with Set-ups B and C. This issue is considered further below.

4.7. The effect of energy-loss on the energy resolution

At this point, it is worth considering the loss of energy resolution expected from the change of the cross-over position with energy-loss. The source size for the Quantum system is the intensity distribution in the PL cross-over plane. This is very small for the zero-loss electrons as it is an image of the probe at the specimen with a magnification of ~20x for the conditions used here. For a very thin specimen, where the highest effective slope corresponds to the probe half-angle, the geometric disc of least confusion has a diameter ~0.3 μm and this rises to ~0.6 μm if the 2.5 mm Quantum aperture is uniformly filled with illumination. Assuming that the object plane of the spectrometer is the plane of the zero-loss cross-over for all energy losses, the spectrometer source size will increase with energy loss because the actual cross-over will move towards the specimen. In line with the normal effect of chromatic aberration, the magnitude of this blurring will depend on the energy loss and the angular range of the ray bundle entering the Quantum aperture. For a very thin specimen, the size of this angular range is defined by the probe angle. As the specimen thickness increases, the angular range will increase due to scattering.

Assuming a very thin specimen, there is a disc in the zero-loss cross-over plane and ray tracing shows that its diameter is ~10 μm per keV of energy-loss. To convert this to a defocus of the spectrum, the relationship between the shift of the source position and the shift of the spectrum is required. Scanning of the probe gives a shift of the zero-loss peak by ~6 eV per micron. The motion of the probe image at the PL aperture plane is ~20x larger and so the zero-loss shift per micron at the PL aperture plane is ~0.3 eV/micron. Thus, for the Si K-edge, at ~1.84 keV, the defocus disc has diameter of 18.4μm at the zero-loss cross-over plane. This corresponds to an energy range of ~5.5 eV Taking the energy resolution as the separation of 10% and 90% points on the integrated profile of uniform disc gives a value of ~5 eV, which should result in some increase in the width of the edge threshold. The 10% to 90% edge resolutions of the Si K-edges in the data used for Fig. 12 are all ~4 eV The appropriate energy resolution of the ZLP to compare to this is the width of the central portion containing 80% of the signal and this is again ~4 eV Thus the width of the Si K-edge has not been broadened in line with the 5 eV prediction. Hence some tilt of the dispersion plane [4] may have been introduced into the Quantum system, minimising the spectrum defocus with energy-loss.

4.8. The effect of energy-loss on the imaging of the pivot points

Turning now to the imaging of the pivot points to the film plane, where the aim is to keep the diffraction pattern stationary on the detectors while the probe is scanned. Even if this is done perfectly, the zero-loss diffraction pattern is only stationary at the film plane and moves slightly at other planes. At sufficiently low magnifications, spherical aberration in the lenses will cause motion of the zero-loss diffraction pattern even at the film plane. With energy-loss, the conjugate plane of the pivot points will move away from the film plane and cause the diffraction pattern to scan there. For STEM-EELS, the plane of interest is the Quantum aperture plane since any motion of the diffraction pattern there will change the signal collection and the collection angles. Fig. 13 shows the shift of the centre of the diffraction pattern in the Quantum aperture plane as the probe moves off axis by up to 5μm. A scan of ±5μm corresponds to a magnification of 20kx on a 20 cm viewing screen.

The motion of the diffraction pattern is largest in Set-up A. When the probe is 5μm off-axis, the centre of the diffraction pattern intersects the 5 mm aperture if the electrons lose 3 keV of

Please cite this article as: A.J. Craven et al., Getting the most out of a post-column EELS spectrometer on a TEM/STEM by optimising the optical coupling, Ultramicroscopy (2017), http://dx.doi.org/10.1016/j.ultramic.2017.03.017

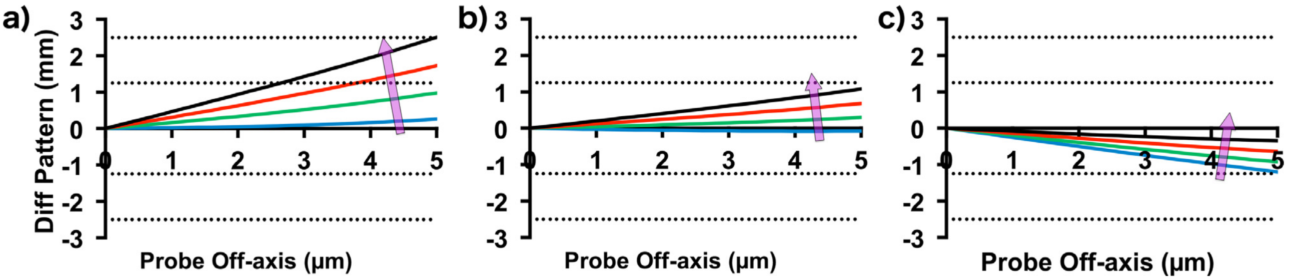

Fig. 13. Motion of the centre of the diffraction pattern in the Quantum aperture plane versus the distance of the probe off-axis. The lines correspond to losses of 0, 1, 2 and 3 keV and the loss increases in the direction of the arrow. The dotted horizontal lines are the positions of the edges of the 2.5 and 5 mm Quantum apertures. a) Set-up A; b) Set-up B; c) Set-up C.

energy. For this probe position, the centre of the pattern also approaches the edge of the 2.5 mm aperture for a loss of 1 keV. In Set-up B, the centre of the pattern only approaches the edge of the 2.5 mm aperture for a 3 keV loss. In Set-up C, the situation is reversed and the 3 keV loss pattern moves very little as the probe scans while it is the centre of zero-loss pattern that approaches the 2.5 mm aperture when the probe is 5μm off-axis.

When the centre of the pattern approaches the edge of the Quantum aperture, the signal entering the spectrometer is approximately halved and so conditions which cause this to happen should be avoided. Imaging the pivot points to the film plane can give a false sense of security when performing spectrum imaging at low magnification. A better way of dealing with this issue is to de-scan the beam immediately after the objective lens, as is done in some instruments. This approach has the added advantage of not scanning the spectrum. However, aberrations will set a limit to the maximum scan size and there may be some chromatic effects in the scan/ de-scan combination.

4.9. Prediction of the performance for higher energy-losses

So far, this paper has concentrated on the energy-loss range 0 to 3 keV since this is both the range over which the diffraction patterns can be recorded and the range into which most EELS falls. However, if the accelerating voltage is lowered, the behaviour discussed so far will occur at lower energy-loss, as discussed in §4.10. There are also some applications where higher energies losses are of interest. One of these is the investigation of oxidation states of metals, which have often been quantified for first row transition elements using the L_3 and L_2 edges [18–20]. More recently this has been extended to zirconium [21] and the aim is to extend this to heavier metals. There is also interest in both the electron near edge structure (ELNES) and extended energy-loss fine structure (EXELFS) for energy-losses above 3 keV. This is normally the province of x-ray absorption spectroscopy (XAS). EELS in this region offers the advantage of higher spatial resolution. For these reasons, it is instructive to look at the predicted projector lens performance over a wider range of energy-loss.

Fig. 14a shows the diameter of the spectrometer object at the PL cross-over plane for zero-loss electrons as a function of energy-loss. This has been calculated assuming a very thin specimen, as above. Combined with the set-up of the Quantum, this will control the energy resolution that can be obtained without re-focusing the spectrum. A more detailed understanding of the combined behaviour of the projector and spectrometer systems is required to predict the actual energy resolution and is beyond the scope of this paper.

Fig. 14b shows the axial position of the PL cross-over as a function of energy-loss. Initially the cross-over is real and after the PL. As the energy-loss increases it moves towards the PL centre. Then it becomes a virtual image and appears before the PL moving off to -∞ as the energy-loss increases. For further energy-loss, it re-appears as a real cross-over at +∞ and starts to move back towards the PL. The curves in Fig. 14b determine by how much the focussing quadrupoles within the Quantum system need to be changed to re-focus the spectrum in order to give the best energy resolution for a given energy-loss. At an energy-loss slightly greater than that required to put the cross-over at ∞, the cross-over becomes conjugate with the Quantum aperture plane. At this point, the camera length is zero. This explains why the intensity band in the camera view goes through a minimum width around this particular energy-loss.

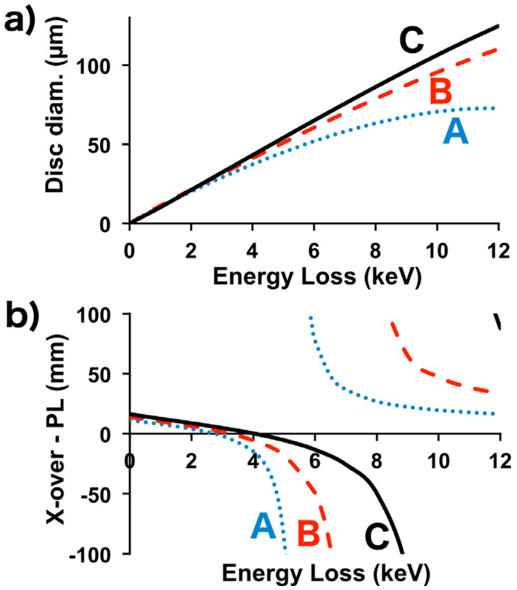

Fig. 14. a) Diameter of the spectrometer object at the PL cross-over plane for zero-loss electrons versus energy-loss. The angular range contributing to the diameter is the 29 mrad probe half angle; b) The distance of the PL cross-over from the PL centre as a function of energy-loss. The labels correspond to the three set-ups.

Fig. 15 shows the position of the rays on the Orius camera as a function of the ray slope at the specimen. The curves are for losses from 0 to 12 keV in 1 keV steps and the energy-loss increases steadily from the bottom curve to the top curve in each plot. The end point of each curve is determined by the maximum value of the ray slope that can pass through the PL aperture. The decrease in the rate of change of camera length with energy-loss on going from Set-up A to Set-up C is marked by the decreasing spacing of the curves at low energy-losses. The curvature of the curves also decreases showing the decrease of the fold-back in the patterns.

The horizontal dashed lines on Fig. 15 show the positions of the 2.5 and 5 mm Quantum apertures projected onto the Orius camera.

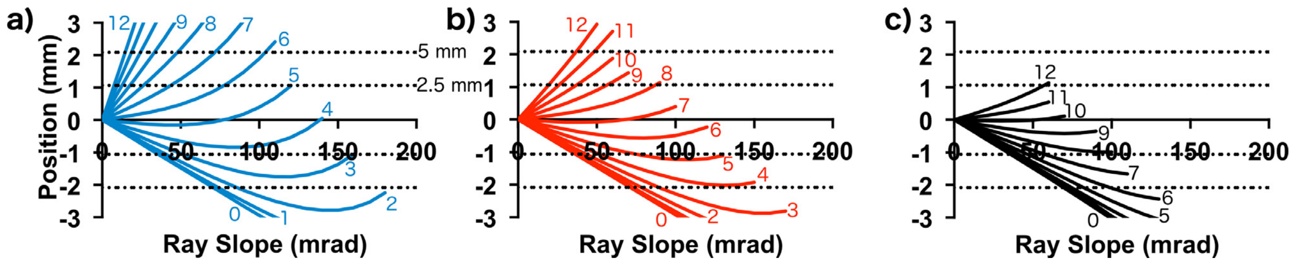

Fig. 15. The radial position of rays on the Orius camera as a function of the ray slope at the specimen. The curves are for losses from 0 to 12 keV in 1 keV increments. Labels are omitted where the curves are too close. The dotted lines correspond to the positions of the edges of the 2.5 and 5 mm Quantum apertures on the Orius camera. a) Set-up A; b) Set-up B; c) Set-up C.

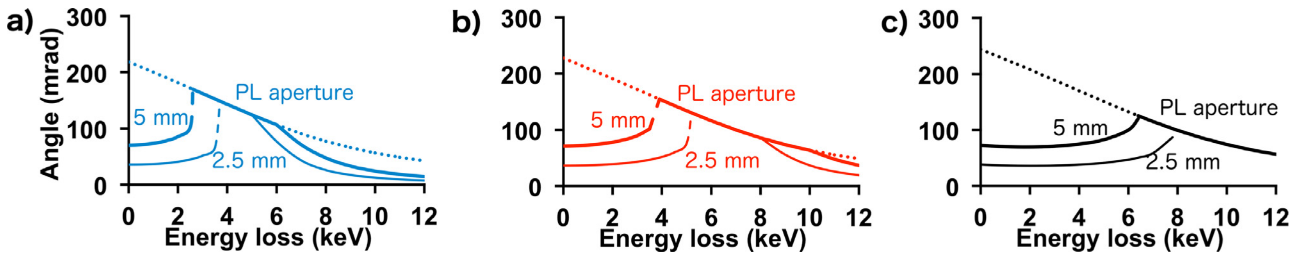

Fig. 16. Collection half-angle versus energy-loss. The thick line is the collection angle for the 5 mm Quantum aperture. The dotted line is the limit imposed by the PL aperture and this is made thick over the energy-loss region for which it is the limit to the collection angle when using the 5 mm aperture. The thin line is the collection angle for the 2.5 mm Quantum aperture and again the PL aperture becomes limiting in the central energy-loss range. The dashed parts of the lines are the regions where the collection angle is not defined by a single number. a) Set-up A; b) Set-up B; c) Set-up C.

Where a curve passes through the position of the lower edge of a Quantum aperture and does not re-cross it at higher ray slope, the Quantum aperture limits the collection half-angle of the spectrometer e.g. in Fig. 15a, curves for energy-losses of 0, 1 and 2 keV fall into this category for the 5 mm aperture. Where the curves lie between the two edges of an aperture, it is the PL aperture that limits the collection half-angle e.g. in Fig. 15a, curves for energy-losses 3, 4 and 5 keV fall into this category for the 5 mm aperture. Where the curves pass through the upper edge of the Quantum aperture, it again becomes the limit e.g. in Fig. 15a, curves with energy-loss of 6 keV or greater fall into this category for the 5 mm aperture.

The transition between the first and second categories differs from that between the second and third categories. For the former transition, the position versus slope can go through a minimum and may re-cross the aperture edge provided it is not cut-off by the PL aperture. In these circumstances, the collection half-angle of the spectrometer is not defined by a single value. However, for the latter transition, the curve always continues to move away from the aperture edge once it has been crossed and so the transition is well defined.

Another way of representing the data is given in Fig. 16, which shows the collection half angle as a function of energy-loss. The thick line is the collection angle for the 5 mm Quantum aperture. The dotted line is the limit imposed by the PL aperture and this is made thick over the range of energy-loss where it is limiting the collection angle when using the 5 mm aperture. The thin line is the collection angle for the 2.5 mm Quantum aperture and again the PL aperture becomes limiting in the central energy-loss range. The dashed parts of the lines are the regions discussed above, where the collection angle is not defined by a single value. They are most extensive for Set-up A because the fold-back of the diffraction pattern is most severe for this set-up. Once this region is reached, the collection half-angle bears little relationship to that measured for zero-loss electrons. For Set-up C, the 2.5 mm Quantum aperture is only just starting to limit the collection angle again at high energy-losses. This is to be expected from Fig. 15c, where the curve for the 12 keV loss only just reaches the position of the 2.5 mm aperture.

The dashed portion of the line for the 2.5 mm Quantum aperture in Fig. 16a for Set-up A shows a very large increase in collection angle in the range which is not defined by a single value. It is this sudden rise in collection angle that results in the anomalous behaviour seen in the spectra recorded using Set-up A in Fig. 12. Fig. 15a predicts that the fold-back will not enter the 2.5 mm Quantum aperture in Set-up A unless the energy-loss is greater than 3 keV. However both sets of data in Fig. 12 show that the perturbation starts to occur for losses greater than 2.6 keV. In the case of the Si data, camera views are available and show a slight misalignment between the centre of the diffraction pattern and the 2.5 mm Quantum aperture. This results in the fold-back entering the aperture at an energy-loss lower than predicted. (Figure S6 in the supplementary material shows line profiles across the camera view, demonstrating this misalignment.) For Set-up B, Fig. 15b predicts that a similar perturbation will only occur for energy-losses greater than 5 keV while Fig. 15c predicts that no perturbation will occur for Set-up C. Whichever set-up is used, care must be taken in the alignment to avoid (or minimise) such artefacts.

The results presented in Fig. 15 can also be used to create schematic simulations of the camera views so that a direct comparison can be made with the camera views in Fig. 3. These are shown in Fig. 17. The black region represents no signal, the grey region represents the signal and the white region represents the fold-back corresponding to that in the diffraction pattern. This fold back increases the intensity in the camera view. In Set-up A this fold-back region is quite wide, while it is much narrower in Set-up B. Fold-back is virtually absent in Set-up C and when it occurs the diffraction pattern is already entirely within the 2.5 mm aperture. Thus it does not cause a perturbation in the spectrum shape other than that caused by the steady change of the collection angle.

The width of the intensity band goes through a minimum in each schematic camera view. The energy at which this occurs experimentally can be found by applying a sufficiently large offset to the magnet current of the spectrometer. These values are compared in Table 2. There is an uncertainty of ∼100 eV in the experimental values due to the broad width of the minimum. The uncertainty in the values from the ray tracing is probably twice this

Please cite this article as: A.J. Craven et al., Getting the most out of a post-column EELS spectrometer on a TEM/STEM by optimising the optical coupling, Ultramicroscopy (2017), http://dx.doi.org/10.1016/j.ultramic.2017.03.017

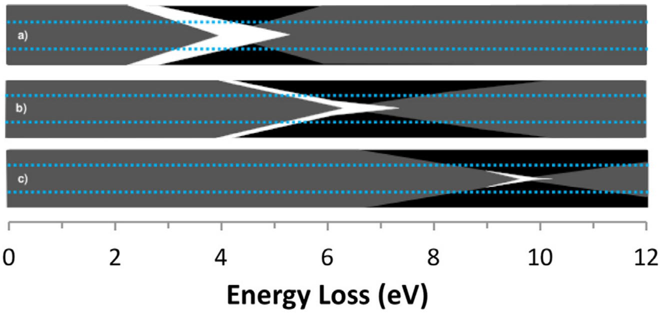

Fig. 17. Schematic camera views based on the data in Fig. 15 (although the scale is not completely accurate) and the width in the vertical direction corresponds to the 5 mm Quantum aperture. The black region is where there is no signal, the grey is the region of normal signal and the white is the region of fold back in the diffraction pattern. The dotted lines show the position of the 2.5 mm aperture. a) Set-up A; b) Set-up B; c) Set-up C.

Table 2
Comparison of the experimentally measured energy at which the intensity band in the camera view passes through its minimum width with that determined from the predictions of the ray tracing for an accelerating voltage of 200 kV. The values for an accelerating voltage of 80 kV are obtained from the 200 kV values using the method in §4.10.

	Set-up A	Set-up B	Set-up C
Experiment (200 keV)	4.8keV	7.4keV	9.2keV
Ray tracing (200 keV)	4.5keV	6.6keV	9.9keV
Ray tracing (80 keV)	1.9keV	2.9keV	4.3keV

since a detailed profile of the intensity band has not been determined.

There is good agreement between the experimental values and those predicted by ray tracing given the uncertainties in both the measurements and the parameters used for the ray tracing. In the ray tracing, thin lens approximations are used for the values of C_c and C_s, resulting in overestimation of the former and underestimation of the latter. In addition, the lens currents have to be adjusted to get agreement between the predicted and observed camera lengths shown in Fig. 4. It is possible that such agreement can be obtained for a number of set-ups and so there may be differences between the actual ray paths and those traced. Nevertheless, all the experimental behaviour is well predicted and so such differences are small.

Thus it is clear that, in seeking to achieve the minimum change of collection angle over the widest possible energy-loss range, two things should be looked for:

- A set-up in which the PL cross-over goes to ∞ at the highest possible energy-loss as this is the key factor controlling the energy-loss range;
- A set-up in which the higher order distortions are minimised and balanced off against each other to avoid or minimise fold-back at the edge of the diffraction pattern. This slows down the change of collection angle with energy-loss and limits the region of ill-defined collection angle as the PL aperture becomes limiting.

One of the reasons for using a 2.5 mm rather than a 5 mm Quantum aperture is clear in Fig. 16, in that it gives a much larger energy-loss range over which the change in collection angle is relatively small. However, if using the 2.5 mm aperture causes a significant loss of signal, it is less desirable. Looking at the camera views in Fig. 3, it can be seen that the width of the signal for the Si K-edge is narrower than the overall width of the intensity band. The signal in the outer part of the band is dominated by the scattering from less tightly bound electrons and so is mainly background. The width of the Si K-edge signal is well matched by the 2.5 mm Quantum aperture. (Figure S7 in the supplementary material shows line profiles across the camera views, confirming this.) Thus the signal to background ratio is improved without significant loss of signal if this aperture rather than the 5 mm Quantum aperture is used.

Table 3
Comparison of the energy-loss ranges over which the collection angle remains within a given percentage of the zero-loss value for an accelerating voltage of 200 kV when using the 2.5 mm Quantum aperture. The figures in brackets are for an accelerating voltage of 80 kV and are obtained using the method in §4.10.

	Set-up A	Set-up B	Set-up C
5%	1.2 (0.5) keV	1.6 (0.7) keV	4.7 (2.0) keV
10%	1.8 (0.8) keV	2.6 (1.1) keV	5.2 (2.2) keV
20%	2.3 (1.0) keV	5.2 (2.2) keV	5.5 (2.4) keV

The data in Fig. 16 can also be used to find the energy-loss ranges within which the collection angles for the 2.5 mm Quantum aperture change by less than a given percentage of the zero-loss value. These are given in Table 3 for 5%, 10% and 20% maximum changes. As expected Set-up A has the smallest energy-loss ranges while Set-up C has the largest. For Set-up C, the offset of the minimum camera length from zero-loss results in a slow variation of collection half-angle with energy-loss followed by a sudden rise. Looking at Table 3, the energy-loss range for a 20% maximum change in collection angle in Setup C is only 20% wider than that for a 5% maximum change. In the case of Set-up B, it is over three times wider while, in Set-up A, it is twice as wide. For smaller percentage changes in collection angle, the energy ranges will shrink and the position of the energy-loss of the minimum camera length must also be considered.

If the collection angle varies with energy-loss, there are potential implications for processing the data. If calculated cross-sections are used, they need to be calculated edge by edge taking into account the collection angle at each energy-loss. If the data is to be deconvoluted, the change in the collection angle across the spectrum may have an effect. For deconvolution to be successful, the low-loss spectrum needs to approximate to that integrated over all angles (see for example the discussion in §4.1.1.5 of Egerton's book [4]). With the large probe and collection angles used here, this is already the case and Fourier ratio deconvolution over a limited energy range is unlikely to be affected, possibly with the exception of data recorded in the energy range in which the collection angle is changing rapidly and by a large amount. For small changes of collection angle, Fourier logarithmic deconvolution is also unlikely to be affected. However, the results will need to be investigated if it is used on spectra that are spliced together to cover a very large energy-loss range.

4.10. Performance at other accelerating voltages

So far the results and discussion are based on an accelerating voltage of 200 kV. In the absence of magnetic saturation effects, which is a reasonable approximation for the projector lenses, the same ray trajectories can be obtained at any accelerating voltage by adjusting the lens current so that $V_R/(NI)^2$ remains the same. Saturation effects cannot be ignored in the objective lens but the current in this lens is carefully set-up at each accelerating voltage to give the correct trajectory for the zero loss electrons. This current is held constant during operation and so the scaling of the focal length for zero loss electrons is always correct.

As a result, the energy scales and specific energy-loss values in the previous sections, which are appropriate for an accelerating voltage of 200 kV, can be converted to those appropriate to any other accelerating voltage.

Please cite this article as: A.J. Craven et al., Getting the most out of a post-column EELS spectrometer on a TEM/STEM by optimising the optical coupling, Ultramicroscopy (2017), http://dx.doi.org/10.1016/j.ultramic.2017.03.017

Provided that $\Delta V_R/V_R$ is the same, the corresponding rays will have the same shapes at any accelerating voltage. In the absence of relativistic effects, $\Delta V_R/V_R$ is equal to $\Delta V/V$. Thus a 0.4 keV loss at 80 kV would give the same ray trajectories and hence performance as a 1 keV loss at 200 kV. From this it is clear that the lower the accelerating voltage, the more challenging it is to study higher energy-losses without a substantial re-design of the post-specimen optics.

As an example of the effect of relativity, V_R at 200 kV is 239.14 kV and, for a loss of 1 keV, ΔV_R is −1.39 kV giving $\Delta V_R/V_R$ of −0.00518. At 80 kV, V_R is 82.26 kV and so, to obtain the same $\Delta V_R/V_R$, the energy-loss must be 0.43 keV i.e. an increase of ~10% over the non-relativistic estimate. In Tables 2 and 3, the values of the energies losses at 80 kV are obtained from those at 200 kV using this method and, as expected, they are all substantially lower. Going to even lower accelerating voltages will make them even lower.

5. Conclusions

It is clear that the performance of an EELS system on a TEM/STEM is very dependent on the set-up of the projector lens system and that the range over which the collection half-angle changes relatively little can be extended significantly with the correct set-up. While this is important for the accelerating voltage of 200 kV used in this work, it is even more important as the accelerating voltage is lowered. Two projector set-ups offering better performance than the standard set-up of a JEOL ARM200CF are identified and their performance compared to that of the original set-up.

First order ray tracing based on matrix multiplication is a good way of searching for set-ups with the required properties. However, these possibilities have to be screened on the microscope itself. For a full description of the behaviour, the effects of spherical and chromatic aberrations must be incorporated into the ray tracing and this can be done by using thin lens approximations. The ray tracing predicts that the maximum diameter of the diffraction pattern is limited with by the aberrations or by the PL aperture. In the former case, the pattern folds back on itself.

The experimental behaviour of the projector system can be explored by offsetting the accelerating voltage while keeping the excitation of the post-specimen lenses constant and observing the diffraction prior to the spectrometer system. The probe must be re-focused on the specimen using the condenser system. The camera view of the spectrum also gives useful information.

All the results from such ray tracing match the experimental results very well provided that the lens settings are fine tuned to get agreement between the experimental and ray traced results for the camera length as a function of energy-loss. The ray tracing explains the form of the spectrum camera view and how it changes with the projector set-up. With this understanding, the experimental conditions can be chosen to maximise performance and avoid artefacts. There are also some minor aberration effects in the Quantum system itself but these have not been investigated.

Two things are crucial in achieving a small change of collection angle over the widest energy range possible. One is to find the set-up which, in addition to meeting the other necessary criteria, also maximises the energy-loss at which the PL cross-over goes to infinity. Experimentally, it is possible to achieve a loss of ~9 keV for this at 200 kV. The other is to find set-ups where, additionally, the deleterious effects of distortion are minimised. For this, higher order distortions resulting from combination aberrations need to be reduced.

There is a correlation between obtaining zero (or low) distortion in the central region of the diffraction pattern and obtaining a maximum in the camera length as a function of energy-loss. Shifting this maximum towards higher energy-loss introduces some positive radial distortion at lower energy-losses and this prevents (or limits) the fold-back of the diffraction pattern. The curvature of the variation of the collection half-angle with energy-loss is also reduced by this. This results in the energy range over which the collection angle is not defined by a single number being eliminated (or minimised).

The ability to choose the energy-loss at which the maximum camera length occurs is useful. In Set-up B, it is at zero and this is useful for EELS at low or medium energy-losses for which a very small change of collection angle with energy-loss is required. In Set-up C, the minimum is at ~2 keV and useful for studying higher energy-losses. With this set-up, the energy-loss range in which the collection angle deviates by a maximum of 5% from the value at zero loss is ~4.7 keV compared with 1.2 keV for the original Set-up A. However if the accelerating voltage is lowered to 80 kV, this range is lowered to 2 keV and it will be even lower at lower accelerating voltages. Further fine tuning of the set-up is possible in order to meet the requirements of a particular investigation.

Despite the shift of the final PL cross-over with energy-loss, the energy resolution does not change as predicted if it is assumed that the dispersion plane of the spectrometer is normal to the axis. This suggests that some tilt of the dispersion plane has been introduced and that this compensates for the shift of the PL cross-over.

The benefits of imaging the pivot points of the scan to the film plane for STEM imaging are lost when energy-loss occurs. The two new set-ups give better performance over a range of energy-loss than the original set-up. Despite giving worse performance at zero-loss, Set-up C gives improved performance as the energy-loss increases whereas the other two give their best performance at zero loss with the performance deteriorating at higher loss. A stationary diffraction pattern for zero-loss electrons can lead to a false sense of security when attempting spectrum imaging at low magnification and this should be approached with caution. De-scanning after the objective lens is a far better way to deal with this issue and also stops the spectrum scanning.

As well as causing changes of collection angle with energy-loss, artefacts can be introduced into the spectrum where the collection angle starts to change rapidly with energy-loss and imperfect alignment can exacerbate such perturbations. Such regions should be avoided if possible. Careful choice of set-up can maximise the energy-loss at which they occur. In the absence of such artefacts, Fig. 12 demonstrates that Fourier ratio deconvolution and spectrum normalisation give the expected results over a range of specimen thickness up to a value of t/λ of 1.5.

As OLK and other workers in the field continue to push the limits of performance of the instrumentation, the coupling of the scattering from the specimen into spectrometer will continue to be an important issue. As smaller probes and lower EHT are pursued, the probe angle will increase e.g. OLK and his collaborators obtained a probe with a diameter of 1.1 Å at 60 kV using a probe half angle of 30 mrad and used this to resolve the carbon atoms in a single layer of graphene [22] while Sawada et al. had to use a probe half-angle in the range 40 – 50 mrad to get similar results at 30 kV [23]. For efficient EELS under such conditions, the collection half angle will have to be increased correspondingly. This larger collection angle, combined with the increased chromatic effects at the lower EHT, will make the optimisation of the coupling a significant challenge. If it has not already been reached, the point is coming where the design of the lens stack itself needs to be optimised for EELS rather than simply optimising the settings of a stack which was designed for imaging and diffraction. The effects of any multi-pole lens between the specimen and the spectrometer must also be taken into account, for instance when an image corrector is present or when a quadrupole-octupole coupling module is used [24]. These issues have not been addressed in the current paper. Thus there is still

Please cite this article as: A.J. Craven et al., Getting the most out of a post-column EELS spectrometer on a TEM/STEM by optimising the optical coupling, Ultramicroscopy (2017), http://dx.doi.org/10.1016/j.ultramic.2017.03.017

considerable work to be done in the field to which OLK has made so many contributions.

Acknowledgements

The authors would like to thank SUPA and the University of Glasgow for funding. Ray Twesten and Paolo Longo (Gatan Inc.), Ray Egerton (University of Alberta), Mhairi Gass (AMEC Foster Wheeler), Wilfried Sigle (MPI für Festkörperforschung, Stuttgart) and Dr Jaco Olivier (Nelson Mandela Metropolitan University) are thanked for helpful discussions about different aspect of EELS during the long period in which we assembled the thoughts that eventually resulted in this paper.

Supplementary materials

Supplementary material associated with this article can be found, in the online version, at doi:10.1016/j.ultramic.2017.03.017.

References

[1] O.L. Krivanek, J.H. Paterson, ELNES of 3d transition-metal oxides I. Variations across the periodic table, Ultramicroscopy 32 (1990) 313–318.
[2] J.H. Paterson, O.L. Krivanek, ELNES OF 3d transition-metal oxides II. Variations with oxidation state and crystal structure, Ultramicroscopy 32 (1990) 319–325.
[3] P.W. Hawkes, E. Kasper, Principles of Electron Optics, Academic Press, San Diego, 1996.
[4] R.F. Egerton, Electron Energy-Loss Spectroscopy in the Electron Microscope, Springer, New York, 2011.
[5] G. Kothleitner, W. Grogger, M. Dienstleder, F. Hofer, Linking TEM analytical spectroscopies for an assumptionless compositional analysis, Microscopy Microanal. 20 (2014) 678–686.
[6] A.J. Craven, J. Bobynko, B. Sala, I. MacLaren, Accurate measurement of absolute experimental inelastic mean free paths and EELS differential cross-sections, Ultramicroscopy 170 (2016) 113–127.
[7] A.J. Craven, T.W. Buggy, Design considerations and performance of an analytical STEM, Ultramicroscopy 7 (1981) 27–37.
[8] D.E. Johnson, Pre-Spectrometer Optics in a CTEM-STEM, Ultramicroscopy 5 (1980) 163–174.
[9] R.F. Egerton, in: R.H. Geiss (Ed.), Analytical Electron Microscopy, San Francisco Press, San Francisco, 1981, p. 235.
[10] P. Kruit, H. Shuman, The influence of objective lens aberrations in energy-loss spectrometry, Ultramicroscopy 17 (1985) 263–267.
[11] J.M. Titchmarsh, T.F. Malis, On the effect of objective lens chromatic aberration on quantitative electron-energy-loss spectroscopy (Eels), Ultramicroscopy 28 (1989) 277–282.
[12] Y.Y. Yang, R.F. Egerton, The influence of lens chromatic aberration on electron energy-loss spectroscopy quantitative measurements, Microsc. Res. Tech. 21 (1992) 361–367.
[13] J. Scott, P.J. Thomas, M. MacKenzie, S. McFadzean, J. Wilbrink, A.J. Craven, W.A.P. Nicholson, Near-simultaneous dual energy range EELS spectrum imaging, Ultramicroscopy 108 (2008) 1586–1594.
[14] A. Gubbens, M. Barfels, C. Trevor, R. Twesten, P. Mooney, P. Thomas, N. Menon, B. Kraus, C. Mao, B. McGinn, The GIF quantum, a next generation post-column imaging energy filter, Ultramicroscopy 110 (2010) 962–970.
[15] K. Evans, R. Beanland, High dynamic range electron imaging: the new standard, Microscopy Microanal. 20 (2014) 1601–1604.
[16] E. Munro, in: P.W. Hawkes (Ed.), Image Processing and Computer Aided Design in Electron Optics, Academic Press, London, 1973, pp. 234–323.
[17] M.E. Haine, V.E. Cosslett, The Electron Microscopy: The Present State of the Art, E. and F.N. Spon, London, 1961.
[18] P.A. van Aken, B. Liebscher, V.J. Styrsa, Quantitative determination of iron oxidation states in minerals using Fe L-2,L-3-edge electron energy-loss near-edge structure spectroscopy, Phys. Chem. Minerals 25 (1998) 323–327.
[19] Z.L. Wang, J.S. Yin, W.D. Mo, Z.J. Zhang, In-situ analysis of valence conversion in transition metal oxides using electron energy-loss spectroscopy, J. Phys. Chem. B 101 (1997) 6793–6798.
[20] L.A.J. Garvie, P.R. Buseck, Ratios of ferrous to ferric iron from nanometre-sized areas in minerals, Nature 396 (1998) 667–670.
[21] K.J. Annand, I. MacLaren, M. Gass, Utilising DualEELS to probe the nanoscale mechanisms of the corrosion of Zircaloy-4 in 350 °C pressurised water, J. Nucl. Mater. 465 (2015) 390–399.
[22] O.L. Krivanek, N. Dellby, M.F. Murfitt, M.F. Chisholm, T.J. Pennycook, K. Suenaga, V. Nicolosi, Gentle STEM: ADF imaging and EELS at low primary energies, Ultramicroscopy 110 (2010) 935–945.
[23] H. Sawada, T. Sasaki, F. Hosokawa, K. Suenaga, Atomic-resolution STEM imaging of graphene at low voltage of 30 kV with resolution enhancement by using large convergence angle, Phys. Rev. Lett. 114 (2015) 166102.
[24] O.L. Krivanek, G.J. Corbin, N. Dellby, B.F. Elston, R.J. Keyse, M.F. Murfitt, C.S. Own, Z.S. Szilagyi, J.W. Woodruff, An electron microscope for the aberration-corrected era, Ultramicroscopy 108 (2008) 179–195.

Please cite this article as: A.J. Craven et al., Getting the most out of a post-column EELS spectrometer on a TEM/STEM by optimising the optical coupling, Ultramicroscopy (2017), http://dx.doi.org/10.1016/j.ultramic.2017.03.017